



**HAL**  
open science

# Effect of Pressure and Turbulence Intensity on the Heat Flux During Flame Wall Interaction (FWI)

Abhijit Padhiary, Guillaume Pilla, Julien Sotton, Marc Bellenoue

## ► To cite this version:

Abhijit Padhiary, Guillaume Pilla, Julien Sotton, Marc Bellenoue. Effect of Pressure and Turbulence Intensity on the Heat Flux During Flame Wall Interaction (FWI). *Flow, Turbulence and Combustion*, 2023, 111 (4), pp.1345-1370. 10.1007/s10494-023-00473-8 . hal-04403575

**HAL Id: hal-04403575**

**<https://ifp.hal.science/hal-04403575v1>**

Submitted on 18 Jan 2024

**HAL** is a multi-disciplinary open access archive for the deposit and dissemination of scientific research documents, whether they are published or not. The documents may come from teaching and research institutions in France or abroad, or from public or private research centers.

L'archive ouverte pluridisciplinaire **HAL**, est destinée au dépôt et à la diffusion de documents scientifiques de niveau recherche, publiés ou non, émanant des établissements d'enseignement et de recherche français ou étrangers, des laboratoires publics ou privés.



Distributed under a Creative Commons Attribution 4.0 International License



# Effect of Pressure and Turbulence Intensity on the Heat Flux During Flame Wall Interaction (FWI)

Abhijit Padhiary<sup>1,2,3</sup> · Guillaume Pilla<sup>2,4</sup> · Julien Sotton<sup>1</sup> · Marc Bellenoue<sup>1</sup>

Received: 25 April 2023 / Accepted: 10 August 2023 / Published online: 1 September 2023  
© The Author(s) 2023

## Abstract

Combustion applications such as internal combustion engines are a major source of power generation. Renewable alternative fuels like hydrogen and ammonia promise the potential of combustion in future power applications. Most power applications encounter flame wall interaction (FWI) during which high heat losses occur. Investigating heat loss during FWI has the potential to identify parameters that could lead to decreasing heat losses and possibly increasing the efficiency of combustion applications. In this work, a study of FWI (CH<sub>4</sub>-air mixture) in a constant volume chamber, with a head-on quenching configuration, at high pressure in both laminar and turbulent conditions is presented. High-speed surface temperature measurement using thin junction thermocouples coupled with high-speed flow field characterization using particle image velocimetry (PIV) are used simultaneously to investigate the effect of pressure during FWI ( $P_{int}$ ) and turbulence intensity ( $q$ ) on the heat flux peak ( $Q_p$ ). In laminar combustion regimes, it is found that  $Q_p$  is proportional to  $P_{int}^{0.35}$ . The increase in  $q$  is shown to affect both  $P_{int}$  and  $Q_p$ . Finally, comparing  $Q_p$  versus  $P_{int}$  for both laminar and turbulent combustion regimes, it is found that an increase in  $q$  leads to an increase in  $Q_p$  ( $b = 0.76$ ).

**Keywords** Flame-wall interaction · Constant volume chamber · Particle image velocimetry (PIV) · Thin junction thermocouples · Heat loss · Turbulence

## Abbreviations

CVC	Constant volume chamber
FWI	Flame wall interaction
HOQ	Head on quenching
IC	Internal combustion
PIV	Particle image velocimetry

✉ Abhijit Padhiary  
apadhiar@exseed.ed.ac.uk

<sup>1</sup> Institut PPRIME, CNRS/ISAE-ENSMA/Université de Poitiers, Chasseneuil du Poitou, France

<sup>2</sup> IFP Énergies Nouvelles, Institut Carnot IFPEN Transports Energie, Rueil-Malmaison, France

<sup>3</sup> Institute for Multiscale Thermofluids, The University of Edinburgh, Edinburgh EH9 3FD, UK

<sup>4</sup> ONERA, French Aerospace Lab, 92190 Meudon, France

RCM	Rapid compression machine
TC	Thermocouple

### List of Symbols

$b$	Exponent of power-law
$c_p$	Heat capacity of fresh gas
$k$	Thermal conductivity of gas
$L_{u,x}, L_T$	Integral length scale
$L_{u,t}, L_{v,t}$	Integral time scale
$Pe$	Peclet number
$P_{int}$	Pressure during FWI
$q$	Turbulence intensity
$Q_P$	Peak Heat flux, during FWI
$Q_\Sigma$	Flame power
$R_{u,t}$	Time correlation function
$S_L$	Laminar flame speed
$t$	Time after spark
$T_{ad}$	Adiabatic flame temperature
$T_{fresh}$	Fresh gas temperature
$U, U_x, U_y$	Velocity, velocity for x component, velocity for y component
$\overline{U_x}, \overline{U_y}$	Mean velocity for x, and average velocity for y component
$u'_{cycle}$	Cycle-to-cycle or shot-to-shot velocity fluctuations
$u'_{HF}$	High-frequency velocity fluctuations
$U_{LF}$	Low-frequency velocity
$u'_{reynolds}$	Velocity fluctuations derived from Reynolds decomposition
$u'_{RMS}$	RMS of turbulent fluctuations
$X_D$	Distance of the wall from the spark plug
$\delta_L$	Laminar flame thickness
$\delta_q$	Quenching distance
$\rho$	Density of fresh gas
$\Phi$	Equivalence ratio

## 1 Introduction

Power generation by conversion of chemical energy of fuels through combustion is still the mainstay (90%, IEA 2021). Most of the combustion applications involve combustion contained in a closed chamber either generating work or heat. IC engines are one such combustion application that has been widely used throughout the last century. Along with conventional fossil fuels, renewable fuels like hydrogen, ammonia, etc. ensure tremendous potential for combustion in future power applications (Senecal and Leach 2021). Heat loss to the walls in such an application is inevitable. In applications like IC engines heat losses range from 10% to over 30% of total fuel energy (Baglione 2007). Hence, it is sought to minimize heat losses to the walls, so that the fuel energy can be used effectively for work (Johnson and Edwards 2013; Kawaguchi et al. 2017; Wakisaka et al. 2016). Heat losses can act as an important lever that has the potential to increase the efficiency of combustion applications, especially in IC engines. Heat losses are

particularly high in the order of MW/m<sup>2</sup> during flame wall interaction (FWI) (Gatowski et al. 1989; Chang et al. 2004; Gingrich et al. 2014; Boust 2006; Dreizler and Böhm 2015).

Simple experiments designed to understand the interaction of laminar flame and wall at low pressures (near 1 bar) have paved the current understanding of FWI. Typically, these experiments are carried out in academic environments like a constant volume combustion chamber (CVC) or a rapid compression machine (RCM). Quenching distance ( $\delta_q$ ) and the peak of heat flux ( $Q_p$ ) are the two most important properties during laminar FWI. A simplified model of laminar FWI (Eq. 1) is presented in the literature where non-dimensional heat flux ( $Q_p/Q_\Sigma$ ) is proportional to the inverse of the pecelet number ( $Pe$ ) (Boust et al. 2007a; Poinot and Veynante 2005).  $Pe$  is typically defined in literature as the ratio of  $\delta_q$  to laminar flame thickness ( $\delta_L$ ). Subsequent studies also adhere to this model, especially on the absolute values of non-dimensional heat flux ( $Q_p/Q_\Sigma$ ) and pecelet number ( $Pe$ ) at quenching which is comprehensively summarized in the review paper (Dreizler and Böhm 2015).

Following Eq. 1, one could derive Eq. 2. Since near adiabatic flame propagation occurs until the instant of FWI, the state properties ( $\rho, c_p, T_{ad}, T_{fresh}, \delta_L$ ) can be defined solely by pressure and gas composition at FWI i.e., the function of pressure ( $P_{int}$ ), fuel, air and equivalence ratio ( $\Phi$ ).  $\rho$  and  $T_{fresh}$  proportional to  $P_{int}^{e1}$ .  $c_p, T_{ad}$ , and  $k$  are a function of  $P_{int}^{e2}$ , fuel–air mixture, and  $\Phi$ .  $S_L$  is typically correlated to  $P_{int}^{e3}$ ,  $T_{fresh}$ , fuel–air mixture, and  $\Phi$  (Metghalchi and Keck 1980, 1982).  $\delta_q$  is also widely correlated with  $P_{int}^{e4}$  in the literature using power-law (Berlad and Potter 1955; Daniel 1957; Goolsby and Haskell 1976; Sotton et al. 2005; Boust et al. 2007a; Labuda et al. 2011). It can be easily derived that  $Q_p$  must be a function of fuel–air mixture,  $\Phi$ , and must be proportional to  $P_{int}^b$ . Equation 3 represents such a possible simplified function. Indeed this analogy is validated through power-law correlations of  $Q_p$  on  $P_{int}$  (Boust 2006; Labuda et al. 2011).

$$\frac{Q_p}{Q_\Sigma} = \frac{1}{1 + Pe} \tag{1}$$

$$Q_p = \rho c_p S_L (T_{ad} - T_{fresh}) / 1 + \left( \frac{\delta_q}{k / \rho c_p S_L} \right) \tag{2}$$

$$Q_p = f(\text{fuel}, \Phi) \times P_{int}^{b(\text{fuel}, \Phi)} \tag{3}$$

Usually, combustion applications like IC engines encounter FWI at high pressures and in environments with high turbulence intensities. This problem can be studied in two incremental steps. First, the laminar FWI is studied at higher pressures (Labuda et al. 2011). The dependency of  $Q_p$  on the pressure during laminar FWI ( $P_{int}$ ) is found as  $Q_p$  proportional to  $P_{int}^b$ .  $b$  is found to be 0.5 when CH<sub>4</sub>-air mixtures at a 1.0 equivalence ratio ( $\Phi$ ) are studied in a rapid compression machine (RCM) with a pressure range of 1 bar to 150 bar (Labuda et al. 2011). In another study,  $b$  is found to be 0.4 when CH<sub>4</sub>-air mixtures at  $\Phi=0.7$  is studied in a CVC with a pressure range from 1 to 25 bar (Boust 2006). RCM is a CVC with a piston that compresses the gas inside RCM to achieve engine-like conditions. In both configurations, a laminar flame propagates towards the wall inducing near adiabatic fresh gas compression. The correlations in both these setups could be qualitatively transferable. It is worth deducing that the variation of  $P_{int}$  is synonymous with the variation of flame power ( $Q_\Sigma$ ) for a fuel–air mixture (constant  $\Phi$ ) as  $Q_\Sigma$  is only a function of  $P_{int}$ . A power-law relationship is a practical way to combine the

dependency of  $Q_p$  on several non-independent parameters which are coupled with  $P_{int}$  ( $Q_\Sigma$ ,  $S_L$ , thermal conductivity of gas, etc.).

Going to the second incremental study of the effect of turbulence on  $Q_p$ , there have been only a few reported works (GRUBER et al. 2010; Poinso et al. 1993; Bruneaux et al. 1996; Boust et al. 2007b). FWI involves a three-way coupling of wall, flame, and flow field where turbulence is expected to play a major role in thermal transport to the wall (Dreizler and Böhm 2015). Although turbulence is shown (through DNS studies in a channel flow) to affect the heat flux to the wall during FWI (by pushing the flame closer to the wall), no such effects have been reported in closed-chamber combustion (Bruneaux et al. 1996). Attempts at separating the influence of turbulence on  $Q_p$  during SWQ in a closed chamber did not yield conclusive results as an increase in turbulence intensity is correlated with the increase in mean velocity and  $P_{int}$  (Boust 2006; Boust et al. 2007b; Sotton 2003). The setup in the concerned study employed a tumbling injection of gas with high speed into a CVC. The faster flame speeds associated with high turbulent intensity ensure different  $P_{int}$  (higher) by just changing the turbulence intensity. At the same time, the method of inducing turbulence employed in the cited work relies on high injection velocity which does not vanish during SWQ events. To understand the FWI in a practical combustion application like engines it is vital to understand the independent effect of the turbulence intensity. Perhaps the coupling of  $P_{int}$  and mean velocity from turbulence intensity is the barrier to understanding the independent effect of turbulence intensity on  $Q_p$ . One possible method to decouple  $P_{int}$  and turbulence intensity could be to present the differences in power-law coefficient ( $b$ ) during laminar and turbulent FWI. Using HOQ configuration could be advantageous as the flow slows down before FWI due to the wall where there is potential for the reduced effect of mean velocity. Hence a study targeting decoupling the effects of  $P_{int}$  and turbulence intensity on  $Q_p$  is proposed in this article.

In this article, we will present the results of experiments on premixed propagative FWI of  $\text{CH}_4$ -air mixtures carried out in head-on quenching (HOQ) configuration in a constant volume combustion chamber (CVC) equipped with a fan for turbulent mixing. The choice of HOQ also merits the existing information that quenching in a HOQ configuration is independent of flame stretch. Rather the quenching is primarily due to heat loss to the walls (Foucher et al. 2003; Foucher 2002).  $\text{CH}_4$  was chosen as fuel for this study because of the availability of a large dataset for  $\text{CH}_4$ -air mixtures including FWI in HOQ configurations in literature (Dreizler and Böhm 2015). FWI in this study is carried out through the interaction of the flame on a flat wall-TC assembly. High-speed surface temperature measurements using thin junction thermocouples embedded in wall-TC assembly are used to derive instantaneous heat flux to the wall using the Duhamel integral (Julien Moussou et al. 2021). Simultaneous PIV is carried out to determine the instantaneous velocity field. Variation in  $P_{int}$  is obtained through a change in the distance of FWI from the spark plug. The effect of  $P_{int}$  on  $Q_p$  is evaluated (a different setup than what is reported in the literature). Using different fan operation strategies in the CVC along with a change in the position of FWI relative to the spark, the effect of turbulence intensity on  $Q_p$  is presented, decoupled from the effect of  $P_{int}$ .

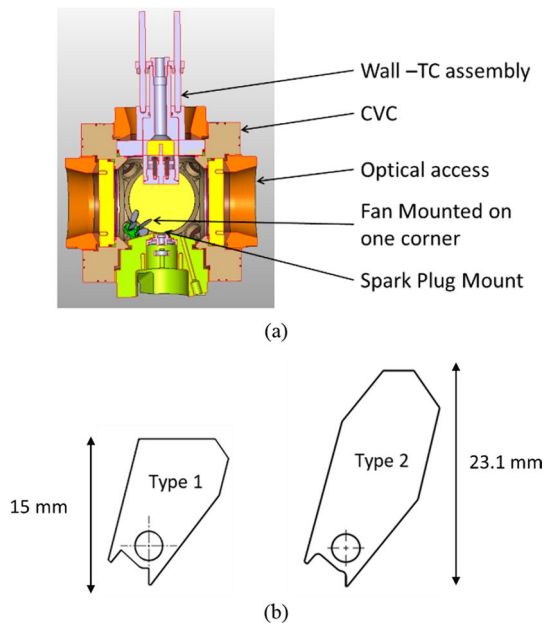
## 2 Methods

In this section, we present the experimental setup, the postprocessing of wall temperature measurements, and PIV.

## 2.1 Constant Volume Combustion (CVC) Chamber

CVC at IFPEN (cross-section is shown in Fig. 1a) is a high-pressure-high temperature CVC typically used in the past to study spray combustion (Pickett et al. 2010). In this work, this CVC is used to study premixed propagative FWI. In a CVC, the initial and boundary conditions (temperature, the composition of combustion gases, etc.) are well controlled to study combustion, providing high repeatability of the experiments. This CVC has 100 mm of inner edge, with optical access through all its faces. The total volume is 1.4 L. The optical accesses are provided with circular optical windows on each face (80 mm in diameter), made of sapphire, to conduct optical diagnostics. During the experiment, the CVC wall temperature is maintained at 473 K ( $\pm 4$  K) or 200 °C ( $\pm 4$  °C), using heating coils and monitoring through embedded thermocouples. The time between experiments (larger than 5 min) is long enough for the CVC to achieve thermal equilibrium before each experiment. In this work, the CH<sub>4</sub>-air mixture at  $\Phi=0.8$  and an initial pressure of 14 bar are used by sequential filling in the CVC. After the filling, the gases are mixed to achieve homogenous composition. For this purpose, a fan (or multiple fans) is used thus introducing turbulence. This feature of introducing turbulence inside CVC through a fan is quite common in literature (Bradley et al. 2019; Galmiche et al. 2013). Two different types of fan blades are used in order, along with the various mode of operations, to obtain various turbulent flows. A schematic of the blades is presented in Fig. 1b. The fans are rotated using a motor shaft connected to a 12-V motor with a target rotation speed (0, 3000, 4000 RPM). A conventional spark plug (with one electrode) is used to initiate the combustion (Denso 5344 IKH20 Iridium Power Spark Plug with 12V, standard coil on plug ignition coil). The pressure inside the CVC during combustion is measured using a piezoelectric pressure sensor, AVL GU21D located on the chamber wall, along with Kistler single channel (Type 5011 B) charge amplifier. During the flame propagation, the pressure in CVC is in equilibrium as

**Fig. 1** a CVC with wall-TC assembly mounted. b Different fan blades used in this study



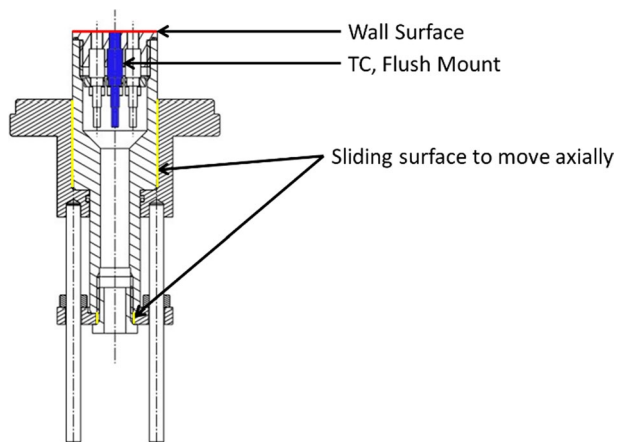
the flame speed is three orders less than the speed of sound. Hence the pressure recording by the sensor at the time of FWI ( $P_{int}$ ) is an accurate representation of pressure at the FWI.

## 2.2 Wall-TC Assembly

Surface temperature measurements are carried out using a fast thermocouple (TC) manufactured by Medtherm Corporation. The TC is a coaxial, K-type, thermocouple with a junction thickness of 1–10  $\mu\text{m}$  and a response time of 1–10  $\mu\text{s}$  (given by the manufacturer). These TC have been used before for surface temperature measurements in engines and CVC (Gingrich et al. 2014; Julien Moussou et al. 2021; Gingrich et al. 2016; Hendricks and Gandhi 2012; Moussou 2019). The output of TC is filtered with a 10 kHz inbuilt filter, which then is amplified using an AD624 amplifier, and gain of 500. The final signal is collected using a Lecroy oscilloscope, sampled at 100 kHz. In an earlier study, a calibration was carried out to determine the response time of the complete surface temperature acquisition chain (Moussou 2019). This calibration was carried out by laser heating yielding a step function of heat flux of 0.2  $\text{MW}/\text{m}^2$ . The response time found is  $0.093 \pm 0.006$  ms. The acquisition chain is expected to perform better with faster response times when TC is exposed to larger heat flux. Hence the response time is considered sufficient to characterize FWI, with a characteristic time of 0.5–1 ms. The TC is embedded in the stainless-steel flat wall (flush mount), designed to mimic the wall during FWI (shown in Fig. 2). The wall has a diameter of 47 mm. The wall-TC assembly has provision to move the wall axially, through hollow support and spacers. Although this wall-TC assembly has provision for multiple TCs, only 1 TC in the center of the wall-TC assembly is used for the present study. In the present study, only HOQ is studied.

Instantaneous heat flux is then calculated from the surface temperature measurement using a 1D semi-infinite model of heat conduction and a Duhamel integral calculation. More details of the heat flux calculation can be found in other related works (Sotton 2003; Moussou 2019). The fast acquisition chain along with Tikhonov regularization ensures that very minimum inaccuracy creeps into heat flux estimation (Hendricks and Gandhi 2012). Very small thermal penetration (in the order of a few  $\mu\text{m}$ ) is estimated for FWI with a typical time scale of 1 ms ensuring high accuracy of heat flux estimation. The supplier-provided

**Fig. 2** Wall-TC assembly and complete setup



effusivity value ( $8500 \text{ W}\sqrt{\text{s}}/\text{m}^2\text{K}$ ) is used for the computation of heat flux. This value is very close to that of a wall made out of stainless steel ( $8000 \text{ W}\sqrt{\text{s}}/\text{m}^2\text{K}$ ). Theoretical upper-bound estimation of the uncertainty associated with heat flux measurements using fast thermocouples as used in this work is found to be up to 5% (Boust et al. 2012). The uncertainty is low compared to the standard deviation within various repetitions of an experiment (typically 10–16% of the mean). The estimated heat flux is reasonably accurate, while the qualitative trends will remain intact.

Examples of two computed heat flux trace from surface temperature are shown in Fig. 3. The surface temperature measured at the wall surface is slightly lower than the CVC temperature as the back side of the wall is exposed to the atmosphere, where some conduction heat loss is possible. The heat flux trace can be decomposed into 5 regions. In Region 1, we can see negligible heat losses 20–30 ms before the first peak. Starting at approximately 20 ms before the first peak is region 2 showing a slow rise in heat flux. The first peak is denoted by Region 3. The heat flux trace then falls to a relatively constant heat flux approximately 10–15 ms after the first peak (region 4). Region 5, starting 15 ms after the first peak, exhibits multiple peaks. The slow rise in Region 2 is attributed to the compression of the fresh gases by the flame. The first peak reaching the order of  $1 \text{ MW}/\text{m}^2$  in Fig. 3, occurs at the time at which the flame reaches the wall, hence it is attributed to FWI (aligns well with literature (Boust 2006)). This has been verified with high-speed  $\text{OH}^*$  imaging and acetone LIF where there is only one peak in the heat flux trace in 10 ms window of the last detected flame front before quenching (Padhiary 2022). The plateau observed in Region 4 is attributed to the high temperature of burnt gas. And finally, the peaks in Region 5 are attributed to turbulent hot gases. Burnt gas-wall interaction is separated from the FWI by a few ms. IC engine operation does not allow the hot gasses to stay inside the engine long enough, so Region 5 is primarily absent. The focus of the current work will be on the first peak due to FWI.

The FWI interaction does not always happen at the same duration after the spark even though all the controllable parameters are kept the same. This could be due to the development of turbulent flame and cycle-to-cycle variations. To draw meaningful statistics for a

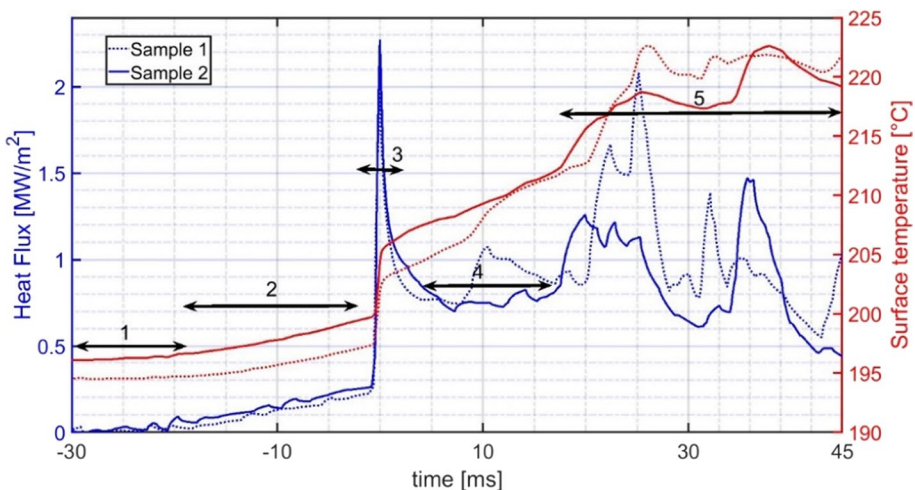


**Fig. 3** Heat flux and surface temperature trace synchronized with respect to  $Q_p$  of FWI for two different repetitions

particular experiment condition (average and standard deviation), we have synchronized the heat flux trace based on the timing of the peak of heat flux (Moussou 2019). Figure 3 shows the result of this synchronization methodology.

Based on the variation of  $Q_p$  we will also find out the number of repetitions necessary for convergence.  $Q_p$  is the maximum heat flux that occurs during the FWI, usually, the first peak in the heat flux trace is in the order of  $1 \text{ MW/m}^2$  or more. In a few cases, instead of one prominent first peak, a group of multiple heat flux peaks close to each other, less than 1 ms of separation in time, is measured. Two examples of such heat flux traces are shown in Fig. 4. Because of delay of 2–3 ms between flame quenching and the heat flux trace it is difficult to estimate which heat flux peak is due to true FWI event. In such cases, the highest peak in the group of closely spaced peaks is chosen as  $Q_p$  during FWI (denoted by circles in Fig. 4. Convergence in averaging  $Q_p$  is reached after 15 experiments, for which the standard deviation is below 5%.

### 2.3 High-Speed PIV Setup

PIV is used in this study to characterize the velocity field. Quantronix Hawk Duo laser is used to generate a laser sheet at a wavelength of 532 nm at 10 kHz to obtain a time series. A set of lenses and a slit of 1 mm thickness is used to get a laser sheet of a thickness of 0.5 mm. A Photron SAZ camera is placed perpendicular to the laser sheet to record the PIV signal with an exposure time of 10 microseconds. A 50 mm objective with a 14 mm ring and f2.8 lens is used in the setup. A bandpass optical filter at  $532 (\pm 4) \text{ nm}$  is used to reduce noise from the flame. A schematic of the PIV setup is provided in Fig. 5.

Solid PIV particles (zirconium oxide) of density  $5800 \text{ kg/m}^3$  and an average size of  $2 \mu\text{m}$  are used in this setup identical to the cited literature (Payri et al. 2016; García-Oliver et al. 2017). The Stokes number estimated is less than 0.2 indicating the PIV particles are good enough to represent the expected flow. The seeding is obtained by passing a part of nitrogen gas through an agitated mesh containing PIV particles. The PIV image is processed with Lavision Davis software to obtain velocity vectors. Particles are determined by subtraction of sliding background (50 Pixels) and then particle intensity is normalized over 9 pixels. Multipass PIV + PTV calculation with hybrid cross-correlation starting from

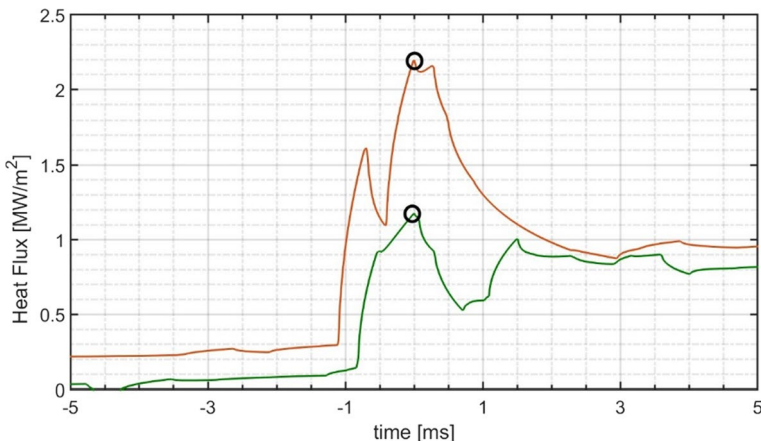


**Fig. 4** Two examples of multi-peak heat flux traces, with highlighted  $Q_p$

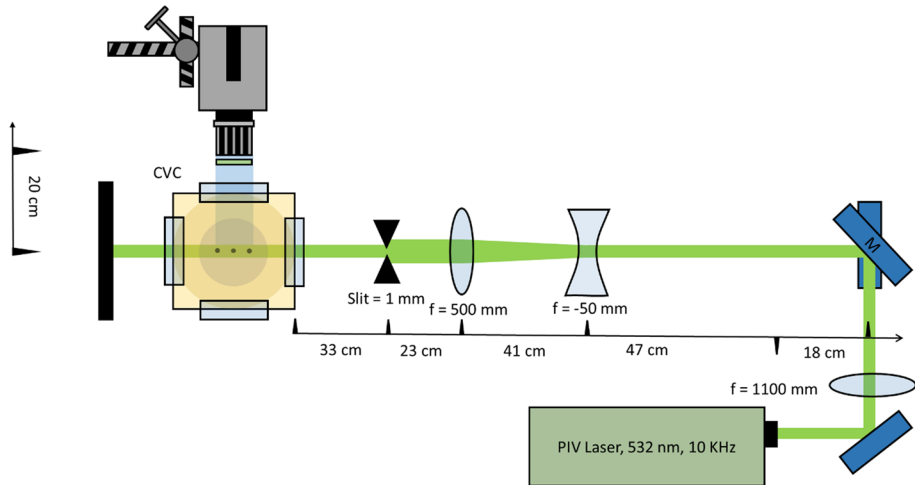


**Fig. 5** Schematic for high-speed PIV

window size of  $64 \times 64$  pixels to window size  $16 \times 16$  Pixels with symmetric shift with 50% overlap and 3 passes. The hybrid algorithm uses PTV in the final step to get maximum resolution for the velocity field. The PIV particle size varies from 1 to 9 pixels in size with a particle density of 0.1ppp or 25.6 bright pixels per  $16 \times 16$  pixels (smallest interrogation window). Vectors are deleted if the correlation value is less than 0.4 or vectors lie away from the average by 3 times the standard deviation (deletion of 1–2% of vectors). Empty vectors are filled up with interpolation among the neighboring vectors. Then a weak filter with a second-order polynomial fit (9 points) is applied. With these operations, the raw image is converted to a velocity vector over space and time i.e.  $\vec{U}(x, y, t)$  with a vector spacing of 0.576 mm. The spatial resolution is estimated to be 0.788 mm. The Davis output files are then managed for post-processing and analysis through open-source PIVMAT MatLab codes (Frederic Moisy 2021). From the time series at 10 kHz, an optimum time duration is chosen for each experiment such that particle displacement is less than 1/4th of the interrogation window size (Padhiary 2022). Overall, the experiment setup and RoI can be seen in Fig. 6 to help better understand the setup. Details of the uncertainty for each type of fan operation and the optimal time duration are given in Sect. 2.5.

The particle density gradient between the fresh gas and burnt gas is used to determine the burnt gas mask. A high-pass Gaussian image filter of size 100 pixels is used to detect the burnt gas mask from the PIV image. An example of the determination of a burnt gas mask is shown in Fig. 6. The low particle density at the border also means that pixel-level detection of the flame front is prone to noise. Because of the low particle density, the velocity field in the burnt gas next to the flame often contains erroneous vectors. Hence, we will only be using the fresh gas velocity vectors for our analysis.

## 2.4 Determination of Turbulence Characteristics from PIV

To derive the turbulence statistics from  $\vec{U}(x, y, t, i)$ , the velocity field needs to be decomposed into average and turbulent components ( $i$  is the repetition of each experiment). Note the time axis for PIV is absolute, i.e.,  $t=0$  is the spark. In literature, Reynolds

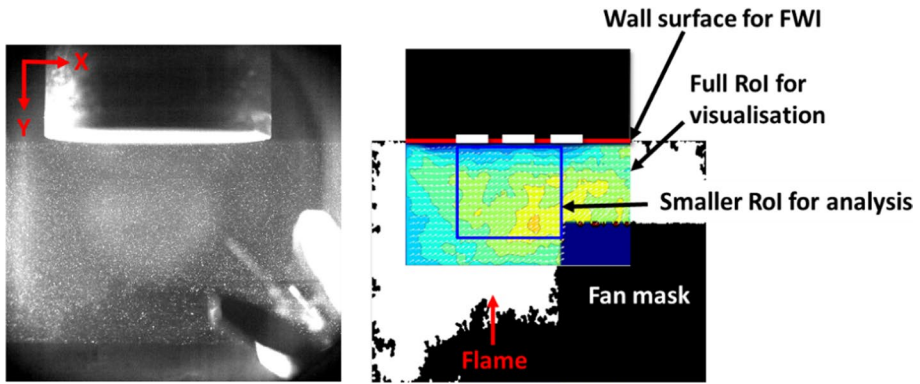


Fig. 6 Schematic of FWI and RoI

decomposition of velocity is frequently used (shown in Eq. 4), where instantaneous velocity,  $\vec{U}(x, y, t, i)$  and ensemble average mean velocity,  $\overline{\vec{U}}(x, y, t, i)$  is used to obtain Reynolds fluctuations  $u'_{\text{Reynolds}}(x, y, t, i)$  (Bradley et al. 2019). However, in applications like a closed combustion chamber, there can be cycle-to-cycle fluctuations in addition to turbulent fluctuations. In such a scenario an alternative method used in literature is to decompose the velocity in the frequency domain i.e., the low-frequency component containing the mean as well as cycle-to-cycle fluctuations, and the high-frequency fluctuations correspond to turbulent fluctuations (Boust 2006; Aleiferis et al. 2017). The decomposition is given in Eq. 5 and Eq. 6.  $u'_{\text{HF}}$  are the high-frequency turbulent fluctuations whereas  $\vec{U}_{\text{LF}}(x, y, t, i)$  is the in-cycle mean velocity consisting of  $\overline{u'_{\text{cycle}}}$ , cycle-to-cycle fluctuations and  $\overline{\vec{U}}(x, y, t)$ , ensemble average velocity.

$$\vec{U}(x, y, t, i) = \overline{\vec{U}}(x, y, t, i) + u'_{\text{Reynolds}}(x, y, t, i) \tag{4}$$

$$\vec{U}(x, y, t, i) = \overline{\vec{U}}(x, y, t) + \overline{u'_{\text{cycle}}}(x, y, t, i) + \overline{u'_{\text{HF}}}(x, y, t, i) \tag{2}$$

$$\overline{\vec{U}}(x, y, t) + \overline{u'_{\text{cycle}}}(x, y, t, i) = \vec{U}_{\text{LF}}(x, y, t, i) \tag{6}$$

The criteria of the cut-off filter are obtained by studying the effect of various temporal window sizes of moving averages in the frequency domain (Aleiferis et al. 2017). Multiple probes (12) in a regular grid in front of the TC are studied. Figure 7 show the Fourier power spectrum density (PSD) distribution of the moving average of instantaneous velocity at one point (2 mm from the TC) with various moving average window size. The PSD of moving averages (different window sizes) of instantaneous velocity separates from the PSD of instantaneous velocity at a particular frequency (shown in the grey band in Fig. 7). This frequency is used as a cut-off frequency for determining high-frequency fluctuations. Conducting such an analysis on each point in space ( $x, y$ ) for each experiment (and repetition) can be a humongous task. Instead, we have used several discrete points in space for one experiment (and repetitions) to yield a range of frequency where the PSD of instantaneous velocity separates from the PSD of the moving

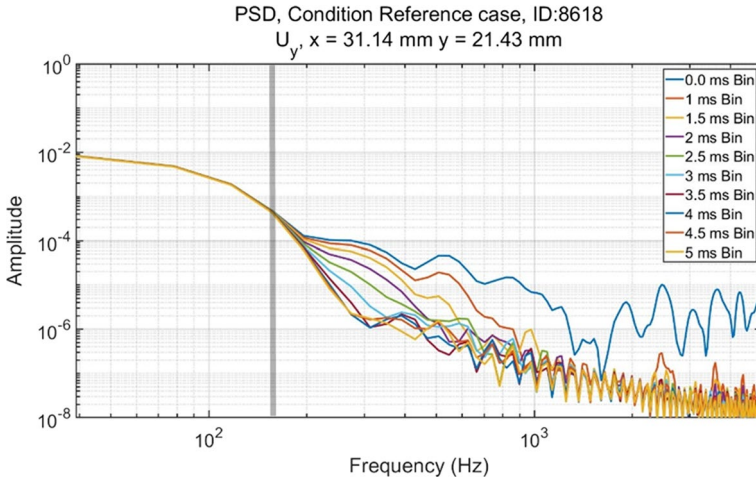


**Fig. 7** Fourier analysis at one point showing the cut-off frequency at which PSD of instantaneous velocity separate from PSD of binned averages for  $U_y$ . Probe is located at 2 mm from the TC

average of velocity. The lowest frequency of the range of cut-off frequency obtained from analysis at different points is used as the cut-off frequency. This cut-off frequency is found as 100 Hz, corresponding to the 10 ms window for the moving average. This cut-off frequency is similar to the order of cut-off frequency used in the literature (Boust 2006; Aleiferis et al. 2017). Using such a method could overestimate the turbulence intensity. However, we will be using flows with highly different turbulence intensities where the slight overestimation of turbulence intensity will not affect the qualitative trends.

Figure 8 shows one example of the velocity field decomposition. In Fig. 8 we can differentiate high-frequency fluctuations (with a small time scale in red color) related to turbulence and the low-frequency instantaneous velocity (in-cycle mean velocity in black color).

Turbulence is found to be isotropic through correlation where  $\overline{u'_x u'_y} = 0$ . Turbulence is found to be homogenous using skewness and kurtosis analysis of turbulence distribution. Observing the time history of turbulence evolution it is found that the amplitude of turbulent fluctuations hardly changes and for any duration sufficient to contain few peaks the mean of  $u'_x$  and  $u'_y$  is zero (less than uncertainty). Turbulence is statistically stationary. A detailed verification is presented in the thesis (Padhiary 2022).

Turbulence is characterized by its length scale and time scale. An autocorrelation method can be used to determine these turbulence characteristics (Kundu et al. 2016). To move from space and time-defined turbulent fluctuations to a representative value for one repetition or a set of experiments, we can obtain the RMS of turbulent fluctuations ( $u'_{RMS}$ ) defined in space and repetitions coordinate as shown in Eq. 7. Each repetition of an experiment is represented by 'i'. The time duration is taken such that flame is not in the smaller ROI of 33 mm  $\times$  23 mm (see Fig. 6). Therefore, wrong vectors near the flame front do not bias the results. The turbulence is quantified in the flow before the arrival of the flame. Statistics are derived from data  $t=2$  ms after spark until the time flame first

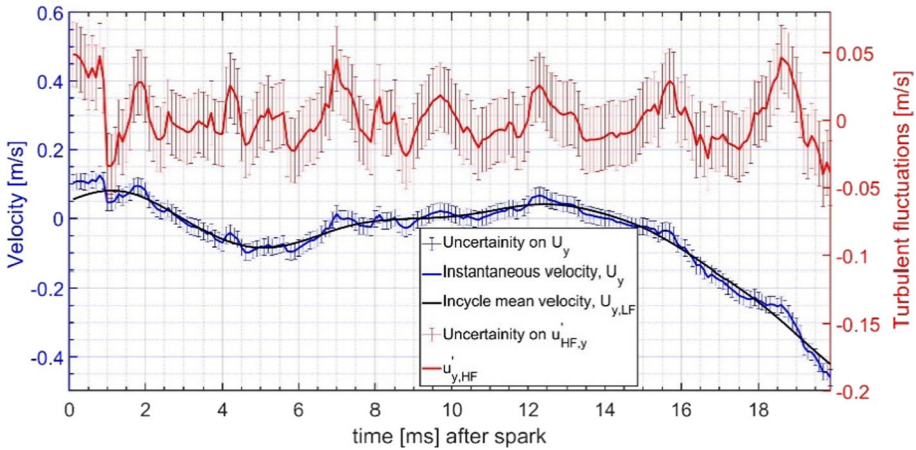


**Fig. 8** Instantaneous, low-frequency, and high-frequency velocity components for one point in RoI for  $U_y$

arrives in RoI, typically over 50 frames to 250 frames, or over a time of 5 ms to 25 ms depending on the experiment.

$$u'_{RMS,x}(x, y, i) = \sqrt{\frac{1}{N} \sum_i u'_x(x, y, t, i)^2} \tag{7}$$

The  $u'_{RMS}(x, y, i)$  is hypothesized to be flat so that a space average of  $u'_{RMS}(x, y, i)$  can give us a representative RMS of turbulent fluctuations for one repetition in a set of experiments as per Eq. 8. A turbulence intensity ( $q$ ) can be computed from  $u'_{RMS}$  of both components shown in Eq. 9. We assume  $u'_{RMS,x} = u'_{RMS,z}$ , which is verified in 2D PIV experiments near the wall (Boust 2006).

$$u'_{RMS,x}(i) = \frac{1}{n} \int \int_{x,y}^{RoI} u'_{RMS,x}(x, y, i) \tag{8}$$

$$q(i) = \sqrt{\frac{u'_{RMS,x}(i)^2 + u'_{RMS,y}(i)^2 + u'_{RMS,z}(i)^2}{2}} \tag{9}$$

The integral time scales of turbulence,  $L_{u,t}$  and  $L_{v,t}$ , are determined by autocorrelation of ‘x’ component velocity and ‘y’ component velocity respectively (Boust 2006; Bradley et al. 2019; Mannaa et al. 2021). The lag in this study is calculated by the method of zero-crossing (Boust 2006). We hypothesize that the time scale over the RoI is flat enough for the spatial average to be representative of each repetition. Spatial averaged integral time scale show that  $L_{u,t} = L_{v,t}$ .

It is determined that the spatial resolution of the experiments is not sufficient to compute the integral length scale by autocorrelation. Alternatively, the length scale is estimated from Taylor’s hypothesis which relates the length scale with the time scale using the mean velocity which is also valid in another CVC setup during the study on FWI (Boust 2006). Further the length scales computed using Taylors hypothesis are only used for indicative

purposes. We have verified from the turbulence time history that the turbulent fluctuations are not affected by flame while the ensemble mean velocity is affected by the flame. Hence, we will estimate the integral length scales using Taylor's hypothesis, at a time, where the ensemble mean velocity is unaffected by flame i.e.,  $t=0$  (at spark) to  $t=5$  ms after the spark.

## 2.5 Experiment Matrix

Experiments presented in this paper are designed with methane ( $\text{CH}_4$ )-air mixture with an equivalence ratio ( $\Phi$ ) of 0.8.  $\text{CH}_4$  is commonly studied for heat losses during FWI (Boust et al. 2007a; Labuda et al. 2011; Sotton 2003). The initial density of  $10 \text{ kg/m}^3$  is chosen to match pressures typical to FWI in engines (Greene 2017). To obtain  $P_{int}$  variation we used three wall-to-spark distances ( $X_D$ ). Different fan types, speeds, and numbers are used to create different turbulence conditions (verified in Sect. 3.2). The complete matrix of experiments is given in Table 1. Since we will present comparisons of different pressure and turbulence variations, notations corresponding to different experiments will be used (Given in Table 1). The *Reference* case represents the case where the fan type and operation used are exactly similar to ECN experiments (Pickett et al. 2010).

For fan operation *LT-XX* series, *Reference*, *HT2-XX*, and *HT3-XX* series optimum time duration between two PIV images are found to be 0.5 ms, 0.3 ms, 0.1 ms and 0.1 ms respectively (Padhiary 2022). The uncertainty of velocity computed from PIV, is 0.014 m/s, 0.024 m/s, 0.071 m/s, and 0.071 m/s for *LT-XX*, *Reference*, *HT2-XX*, *HT3-XX* series respectively. It is also later found, in Sect. 3.2., that *LT-XX* series is laminar regimes while *HT2-XX* and *HT3-XX* series lie in turbulent combustion regimes.

**Table 1** Experiments carried out in CVC

CH <sub>4</sub> -Air at 0.8 $\Phi=0.8$ at $10 \text{ kg/m}^3$ , initial CVC temperature = 473 K, initial pressure = 14 bar					
Fan blade type	No. of fans	Fan speed at $t=0$ RPM	Fan operation	$X_D$ mm	Notation
Type 1	1	3000	OFF 60 s before spark	30	<i>LT-30</i>
Type 1	1	3000	OFF 60 s before spark	60	<i>LT-60</i>
Type 1	1	3000	OFF 60 s before spark	80	<i>LT-80</i>
Type 1	1	3000	Always ON	60	<i>Reference</i>
Type 2	2	4000	Always ON	30	<i>HT2-30</i>
Type 2	1	4000	Always ON	60	<i>HT2-60-1F</i>
Type 2	2	4000	Always ON	60	<i>HT2-60</i>
Type 2	2	4000	Always ON	80	<i>HT2-80</i>
Type 2	3	4000	Always ON	30	<i>HT3-30</i>
Type 2	3	4000	Always ON	60	<i>HT3-60</i>
Type 2	3	4000	Always ON	80	<i>HT3-80</i>

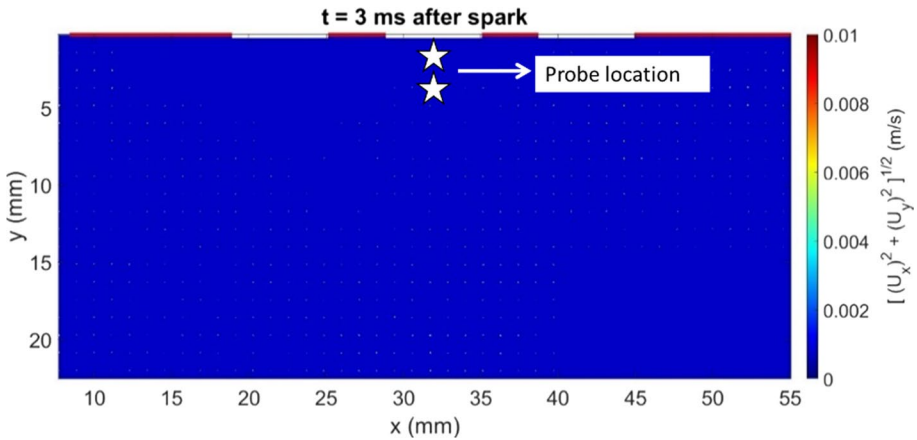


**Fig. 9** Flow field for *LT-60* after flame affects the flow field. Probe location for Fig. 11

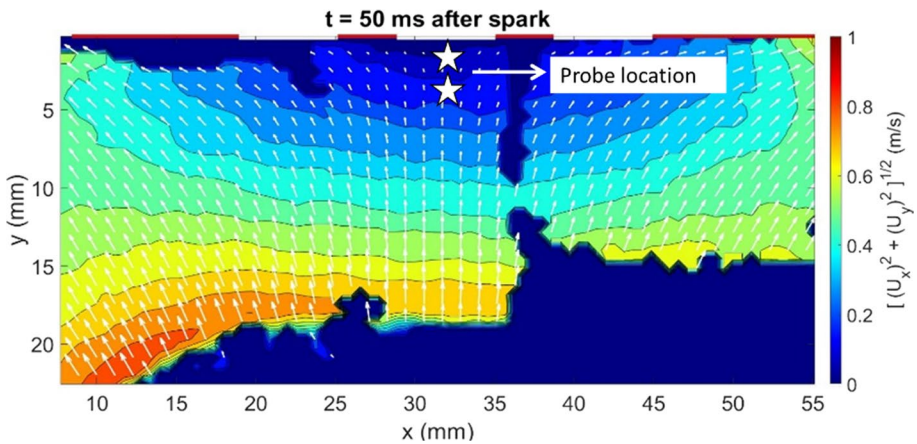


**Fig. 10** Flow field for *LT-60* at  $t=50$  ms after spark when flame affects the flow field. Probe location for Fig. 11

### 3 Results and Discussions

#### 3.1 Aerodynamics Characterization

Four types of fan operations and two types of fan blades are used to generate variations in aerodynamics inside the CVC. The details of the fan operation and the corresponding notation are given in Table 1.  $t=3$  ms after the spark is chosen as the representative time for the flowfield at the time of spark ( $t=0$  ms) to remove the border effects of the filters used for processing the flow field.

At  $t=3$  ms after spark, the flow field for *LT-60* is quiescent (shown in Fig. 9, where velocity magnitude is  $<0.01$  m/s). Nevertheless, sometime after the spark ( $t=50$  ms), the flame-induced flow field is seen (shown in Fig. 10) indicating that the flow is significantly

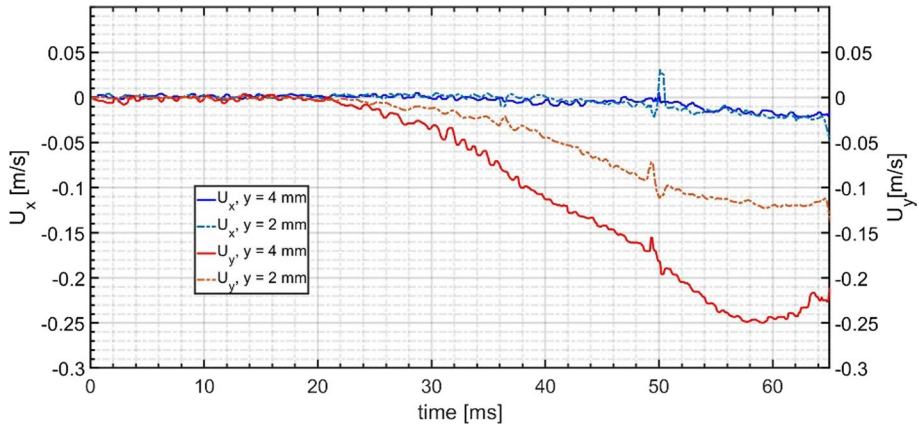


Fig. 11 Instantaneous flowfield at one point in space with  $y$  distance from the center of the wall, for *LT-60*

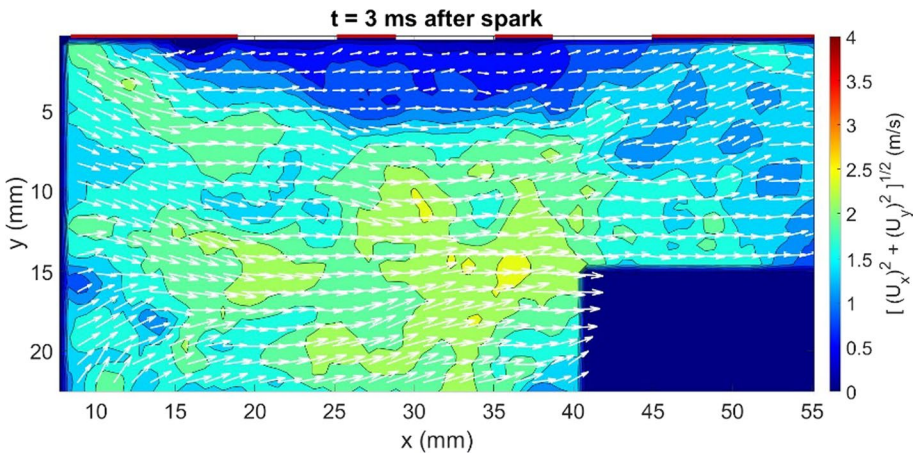
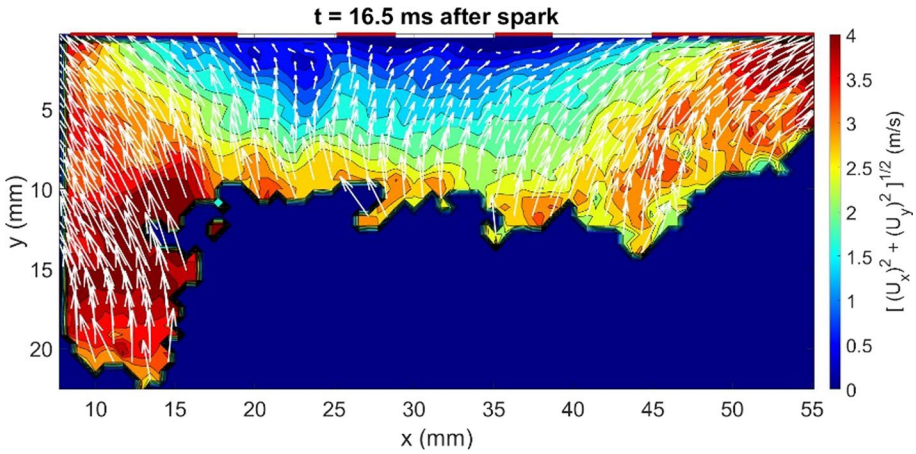


Fig. 12 Flow field in *HT2-60* case with 2 fans at  $t = 3$  ms after spark. The three white bar are the surface TCs

affected by the flame propagation. Mean velocities for *LT-60* ( $\overline{U_x}, \overline{U_y}$ ) evaluated at two positions at the center of the wall (2mm and 4mm from the wall in front of TC) are shown in Fig. 11. It is seen that the magnitude of  $\overline{U_y}$  increases as the flame approaches the wall. However, after a certain time, the magnitude of  $\overline{U_y}$  decreases again. As reported in the literature, such behavior may be attributed to the deceleration of the flame close to the wall found in FWI events in a CVC at atmospheric pressure (Boust 2006; Sotton 2003). These observations are common to both the points of observation at the center of the wall ( $y = 2$  mm and 4 mm normal to the wall). The trend observed at these two locations (shown in Fig. 11) is common for all locations in RoI.

Except for *LT-60*, at  $t = 3$  ms (close to the spark timing), the flow is parallel to the wall for all other cases. The flow behavior at different times after the spark for *HT2-60* for RoI is shown in Figs. 12, and 13. In Fig. 12, at  $t = 3$  ms after the spark, the flow field is parallel



**Fig. 13** Flow field in *HT2-60* case with 2 fans at  $t = 16.5$  ms after spark

to the wall (imposed by the fan) is seen. The velocity parallel to the wall ( $U_x$ ) is decreasing in the order, *HT3-60* > *HT2-60* > *Reference*. At  $t = 13$  ms and 16.5 ms (in Figs. 12 and 13 respectively), the flow field appears to be affected by the flame leading to a jet-wall impingement type of flow. Similar results have already been observed in engines (Greene 2017). The velocity normal to the wall ( $U_y$ ) increases during this time just like in *LT-60*. This modification of flow velocity is common to all fan operations used in this paper. This effect of flame takes place much before flame enters the field of view. After the flame affects the flow, the flow starts to become normal to the wall. The absolute velocities ( $U_y$ ) vary in order *HT3-60* > *HT2-60* > *Reference* > *LT-60*. The velocity parallel to the wall ( $U_x$ ) rearranges to accommodate jet wall impingement flow.

Mean velocities ( $\overline{U_x}$ ,  $\overline{U_y}$ ) evaluated at two positions ( $y = 2$  mm and 4 mm from the center of the wall) are shown in Fig. 14 for *HT2-60*. These observations are like what has been

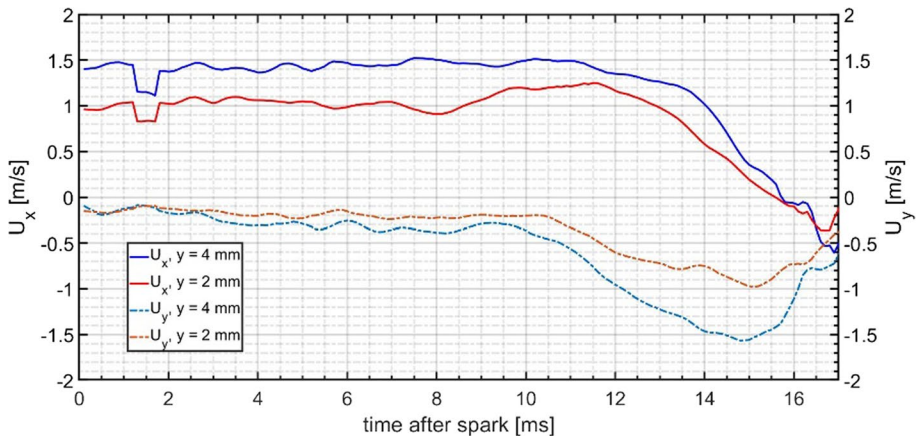


**Fig. 14** Instantaneous flowfield at one point in space,  $y$  is the distance from the center of the TC (*HT2-60*). The probe locations are same as Figs. 9, 10, and 11

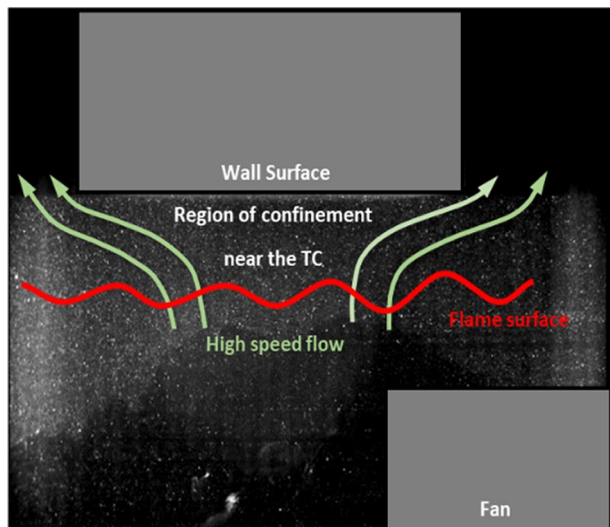
found in the case of *LT-60* despite all *HT2-60*, and *HT3-60* cases having much stronger velocities at  $t=3\text{ms}$ .  $\overline{U}_x$  for *HT2-60* also shows a change in a direction apart from the magnitude (shown in Fig. 14). Overall, there exists a region of low overall  $\overline{U}_x$  and  $\overline{U}_y$  (in magnitude), which is due to the confinement of the flow by the wall (seen in Figs. 13 and 10) and flame. A schematic of the flow field is given in Fig. 15. In this figure, we can see the region of confinement near the TCs. This region of confinement is about 5 mm from the TC and does not show any variation for different fan operations and  $X_D$ .

Although it is established that a region of confinement exists during FWI leading to a decrease in velocity, we need to find to what extent the velocity decreases. Hence, we analyzed the flow field just before FWI in detail by tracing velocity till the instant of flame arrival at a point of observation or probe. For this purpose, the spatial location of  $y=2\text{ mm}$  from the center of the wall (first probe in Figs. 9 and 10) is chosen as the probe.

We choose to present experiment *HT2-60* to illustrate the analysis. The instantaneous velocity as a function of time at the probe is shown in Fig. 16. The flame's arrival at the probe (in time) is denoted by a circular marker. For some of the repetitions (6/14 repetitions for  $U_y$  and 5/14 repetitions for  $U_x$ ), we can trace the deceleration fully until the magnitudes of  $U_x$  and  $U_y$  decrease below 0.5 m/s (Case 1). For this operating condition, the amplitude of the turbulent fluctuations is 0.5 m/s. Hence, we conclude that the magnitude of  $U_x$  and  $U_y$  falls to the level of turbulent fluctuations. This decrease in the magnitude of velocity is attributed to the confinement of the fresh gas near the wall where it can only be compressed (rather than getting pushed). Hence leading to the only possibility of monotonous decay in both  $U_x$  and  $U_y$  until FWI.

For the rest of the repetitions, we can trace either only a part of the deceleration where  $U_x$  and  $U_y$  fall in magnitude but not exactly down to 0.5 m/s (4/14 repetitions for  $U_y$  and 6/14 for  $U_x$  denoted as Case 2) or that the magnitude of  $U_x$  and  $U_y$  fell to less than 0.5 m/s and then increased to a small value above 0.5 m/s (4/14 repetitions for  $U_y$  and 3/14 for  $U_x$ , denoted as Case 3). Following from the previous paragraph that the magnitude  $U_x$  and  $U_y$  can only follow monotonous decay due to the 'region of confinement' until FWI, the slight

**Fig. 15** Schematic of the flow field prior to FWI



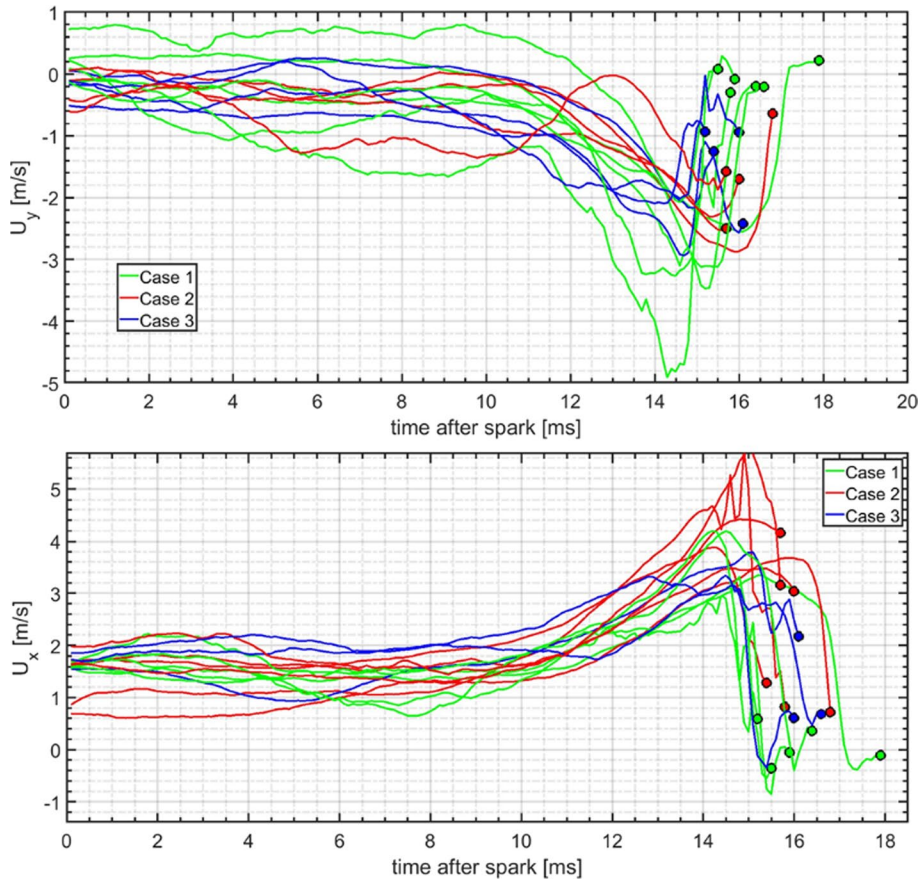


**Fig. 16** Instantaneous velocity at  $y=2$  mm from the center of the TC for HT2-60. Top, x component instantaneous velocity,  $U_x$ . Bottom y component instantaneous velocity,  $U_y$

increase in the magnitude of  $U_x$  and  $U_y$  is fictitious. We hypothesize this fictitious increase is due to limitations of using PIV particle density to detect the flame front (noise in burnt gas mask determination, as discussed in Sect. 2.3). Hence, we conclude that the magnitude of  $U_x$  and  $U_y$  for all experiments and repetitions reaches the magnitude of  $u'_x$  and  $u'_y$  in the region close to the wall just before FWI. This implies that  $\bar{U}_x$  and  $\bar{U}_y$  are 0 m/s close to the wall before FWI.  $Q_p$  is not influenced by mean velocity for the different experiments of turbulence variation conducted in this paper.

### 3.2 Turbulence Levels Achieved in the Setup

Different turbulence intensities affect the propagation of the flame in the CVC (Poinot and Veynante 2005). Hence, the different experiments corresponding to different turbulence variations shown in Table 1 lead to different pressure evolution (and different  $P_{int}$ ) in the CVC. A direct comparison of  $Q_p$  for different experiments is only possible if we obtain  $Q_p$  for a range of  $P_{int}$  for all experiments and then compare the resulting  $Q_p$  vs

$P_{int}$  curves. The turbulence intensity ( $q$ ) is computed from PIV, using the methodology described in Sect. 2.3, for all the experiments for times when the flame is far from the RoI ( $t=50\text{--}100$  ms for  $HT2/HT3$ ,  $t=50\text{--}200$  ms for the rest). The results are presented in Fig. 17. We achieve major change in  $q$ , up to two orders of magnitude (1000%), due to variations in fan operation ( $LT-XX$  to  $HT2-XX$ ,  $HT3-XX$ , ‘XX’ stands for different  $X_D$ ).  $X_D$  variations induce negligible change in  $q$  (50–100%) in comparison to the variation in  $q$  induced by different fan operations. The uncertainty of turbulence intensity computed derived from the uncertainty of velocity computed from PIV, is 0.014 m/s, 0.024 m/s, 0.071 m/s, and 0.071 m/s for  $LT-XX$ , *Reference*,  $HT2-XX$ ,  $HT3-XX$  series respectively. One of the limitation of the current study is the some what large variation in the computed shot-to-shot turbulent intensity.

The relative strength of turbulence (intensity and length scales) to that of laminar flame (laminar burning velocity and laminar flame thickness) is often used to define various combustion regimes (Poinso and Veynante 2005). Using Cantera (GRI 3.0 Mechanism), the laminar flame properties are computed for the used gas composition and  $P_{int}$  found in each experiment (Goodwin et al. 2017). Based on the calculation of turbulence properties, i.e., integral length scale and turbulent intensity, all the experiments in Table 1 are placed in the combustion regimes diagram in Fig. 18 (Poinso and Veynante 2005). The shaded portion in Fig. 18 indicates the domain of turbulence encountered in typical IC engines (Gianfilippo Coppola et al. 2009). Placing the experiments of Table 1 in the combustion regime diagram we see that  $HT2-XX$  and  $HT3-XX$  are very close to that domain, while  $LT-XX$  lies in laminar flame regimes. This confirms that the experiments conducted in the present work are representative of the IC engine conditions. It should be noted that the placement of experiments in the combustion regimes diagram is only accurate immediately prior to FWI. At FWI, the laminar flame properties may be affected by the wall which cannot be estimated in this work.

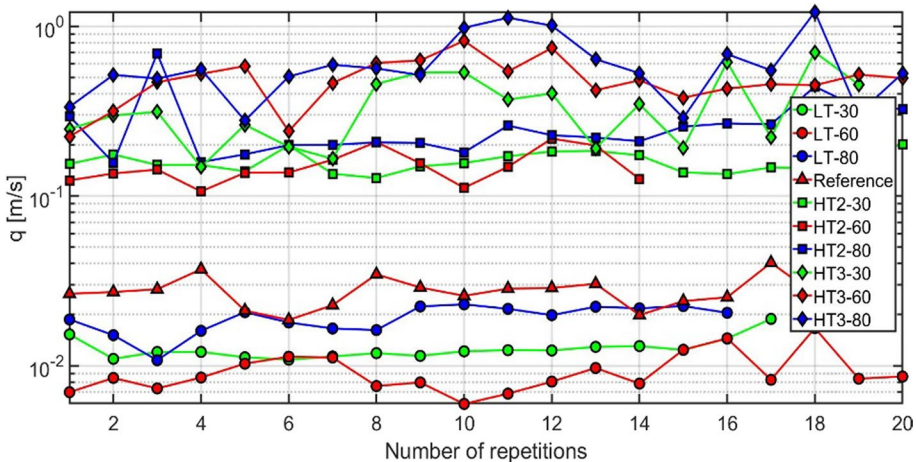
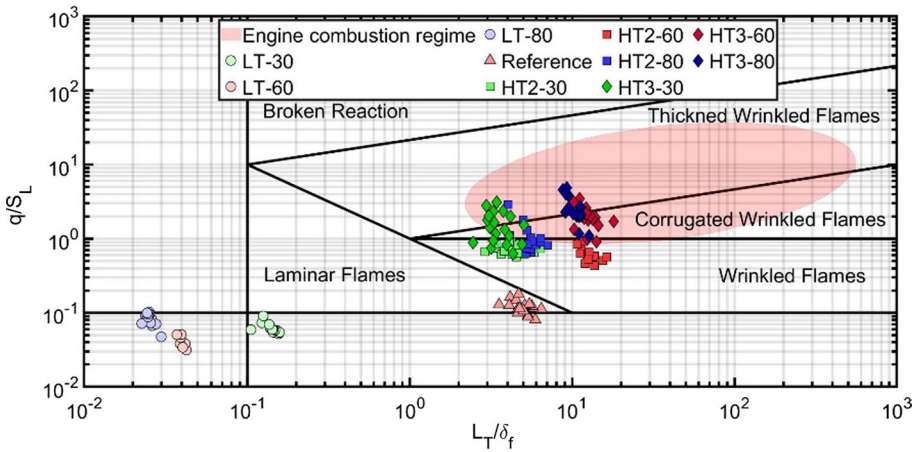
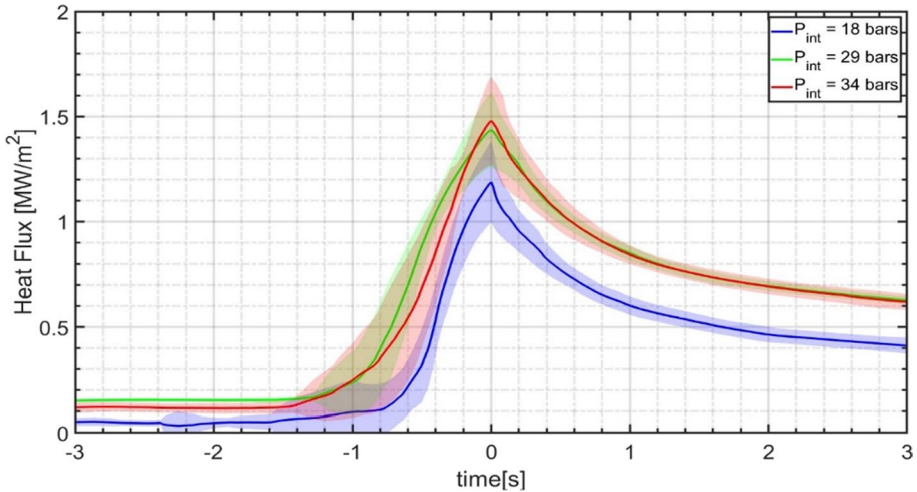


Fig. 17 Turbulence intensity ( $q$ ) for experiments in Table 1



**Fig. 18** Different regimes of combustion achieved during experiments in CVC with different fan operations



**Fig. 19** Effect of  $P_{int}$  on  $Q$  for different  $X_D$ . Solid lines represent the mean while shaded lines represent the standard deviation (15 repetitions for each experiment)

### 3.3 Effect of Pressure During Laminar FWI

With the strategy to use variation in  $X_D$  to obtain variation in  $P_{int}$ , the effect of  $P_{int}$  on  $Q_p$  for our experiments can then be determined. Figure 19 presents the heat flux traces obtained for the laminar cases ( $LT-30$ ,  $LT-60$ , and  $LT-80$  shown in Table 1). It can be seen that  $Q_p$  increases with  $P_{int}$  between 18 and 34 bar.

Using a method of minimization of error, we can use  $Q_p$  to obtain the power-law coefficients which are given in Eq. 10 and shown in Fig. 20. The limitation of the current study is that we only have three variations in  $X_D$ . However, the power-law relationship is well

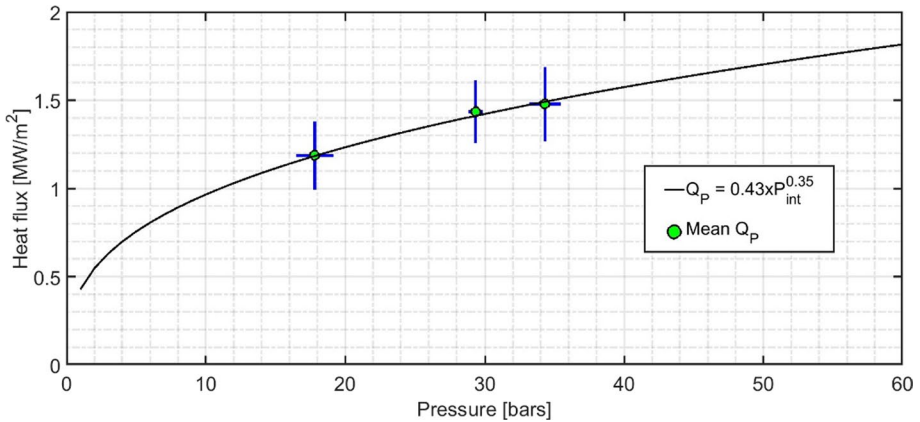


Fig. 20 Power-law dependency of  $Q_p$  on  $P_{int}$  for laminar case

established in the literature for pressure ranges from 1–150 bar in RCM and up to 1–25 bar in a CVC justifying its usage.

$$Q_p(\text{MW}/\text{m}^2) = 0.43 \times P_{int}(\text{bar})^{0.35} \tag{10}$$

The coefficient  $b$  obtained in our experiments ( $b=0.35$ ) is slightly different from the one obtained in the literature ( $b=0.5$  at  $\Phi=1$  in RCM and  $b=0.4$  at  $\Phi=0.7$  in CVC). The difference in  $b$  obtained in this work and literature is small and possibly a larger dataset of experiments could lead to closer agreement with literature. There are only a few studies that explore the power-law relationship (Eq. 10), as such we cannot identify the difference in  $b$  (Boust 2006; Labuda et al. 2011). Using the qualitative derivation shown in Eq. 3, we hypothesize that this difference in magnitude of  $b$  could be primarily due to different gas compositions, initial wall temperature, initial gas density, and experiment configuration. We also hypothesize that for experiments where composition, wall temperatures, and experiment configurations are kept constant,  $b$  remains the same. The power-law relationship established in Eq. 10 and now be used to separate the effect of  $P_{int}$  and isolate the effect of other parametric variations.

### 3.4 Effect of Turbulence Intensity on QP

Now we present the dependency of  $Q_p$  on  $P_{int}$  for the experiments presented in Table 1, with the objective being to understand the influence of  $q$  on  $Q_p$ . To analyze turbulent combustion, we need to study the dependency of  $Q_p$  on  $P_{int}$  in both laminar and turbulent combustion regimes (shown in Fig. 21),  $Q_p=f(P_{int}, q)$  where  $q$  is near zero for laminar cases. The corresponding  $P_{int}$ ,  $q$ , and  $Q_p$  data are also shown in Table 2. Compared to the laminar regimes (*LT-XX*),  $P_{int}$  for turbulent regimes (for the *HT2-XX* and *HT3-XX* series of experiments) are not well separated for different variations in  $X_D$ , forming a continuous scatter. This scatter is due to shot-to-shot variation in flame arrival at the wall leading to scatter in  $P_{int}$ . The overall scattering in *HT2-XX* and *HT3-XX* is much larger than *LT-XX*.

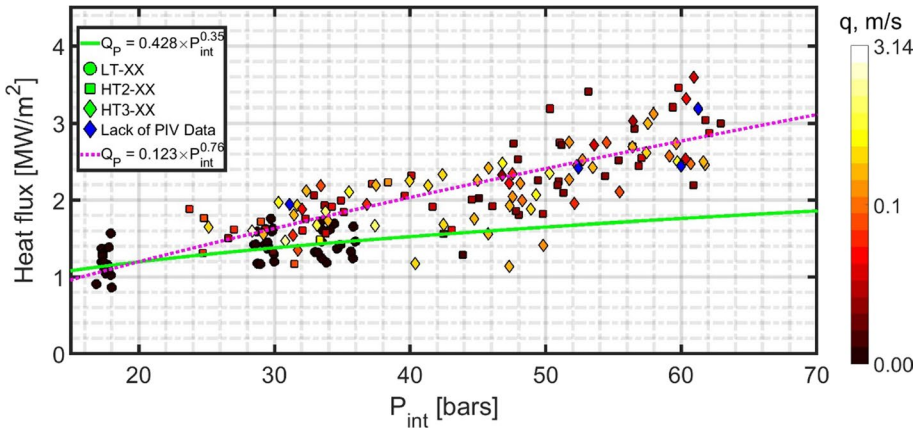


Fig. 21 Dependency of  $Q_p$  on  $P_{int}$  for different regimes of combustion (scatter)

Table 2  $P_{int}$ ,  $q$ , and  $Q_p$  for experiments in Table 1

Experiment notation	$P_{int}$ bar	$q$ m/s	$Q_p$ MW/m <sup>2</sup>
LT-30	17.5 ± 0.3	0.013 ± 0.002	1.17 ± 0.18
LT-60	29.3 ± 0.5	0.010 ± 0.003	1.44 ± 0.18
LT-80	34.3 ± 1.1	0.019 ± 0.003	1.45 ± 0.18
Reference	37.6 ± 3.3	0.028 ± 0.006	1.90 ± 0.21
HT2-30	31.3 ± 4.6	0.159 ± 0.021	1.76 ± 0.30
HT2-60	46.2 ± 3.9	0.151 ± 0.030	1.91 ± 0.28
HT2-80	55.4 ± 5.0	0.266 ± 0.057	2.76 ± 0.41
HT3-30	34.0 ± 4.7	0.350 ± 0.150	1.86 ± 0.27
HT3-60	49.4 ± 4.6	0.500 ± 0.144	2.04 ± 0.38
HT3-80	58.3 ± 3.1	0.560 ± 0.132	2.80 ± 0.35

Although the shot-to-shot scatter on  $q$  is not directly correlated to  $Q_p$ , the mean tendency show that increase in  $q$  leads to increase in  $Q_p$ . Further, we can find that for same  $X_D$  LT-XX cases register a lower  $P_{int}$  compared to HT2-XX and HT3-XX. At low  $P_{int}$ , the difference between  $Q_p$  for turbulent FWI and  $Q_p$  for laminar FWI is small. The mean values of  $Q_p$  for turbulent regimes at  $X_D = 30$  mm is 20–27% higher than  $Q_p$  for laminar regimes at  $X_D = 60$  mm and 80 mm at low  $P_{int}$ . However, higher  $P_{int}$  data for laminar FWI is not available due to limitations of the current experimental setup where higher  $P_{int}$  is not achievable for laminar configuration. We must rely on the power-law relationship for laminar FWI (Eq. 10). Such a power-law relationship is found to be valid across a large range of  $P_{int}$  (1 bar to 150 bar) by past researchers, although in different setups (Labuda et al. 2011). A power-law fit on all scatter for HT2-XX and HT3-XX gives  $b = 0.76$  which is greater than the value of  $b$  (0.35) obtained for laminar regimes. The mean error between predicted and experimental  $Q_p$  obtained with power-law fit is 24%.

In Fig. 21, there is a scatter in  $Q_p$  for the turbulent case leading to the five repetitions of turbulent combustion experiments where  $Q_p$  is lower than that of the laminar case. These special cases register a multi-peak heat flux profile (shown in Fig. 4). Other multiple peak

heat flux traces have a higher  $Q_p$  than *LT-XX* trendline, hence not highlighted. The multi-peak heat flux profile perhaps has a link to turbulence leading to high shot-to-shot variation in  $Q_p$  for *HT2-XX* and *HT3-XX* cases. We have two hypotheses that could lead to such multiple peak heat flux traces. First, such multiple peaks could be due to flame front fluctuations or instabilities near the wall which could lead to multiple FWI events corresponding to different peaks. Second, flame fragments could convect near the sensor leading to multiple flame front interactions and multiple peaks. We are limited by the spatial resolution to investigate it further (integral length scales computed using Taylor's hypothesis are less than the spatial resolution of PIV).

In spite of the scattering, this representation of  $Q_p$  as a function of  $P_{int}$ , and  $q$ , show that turbulent FWI leads to an increase in  $Q_p$  beyond the effect of  $P_{int}$  alone. To our knowledge, such effects of turbulence intensity on  $Q_p$  have not been reported in the literature in closed chamber FWI studies. This adds to other studies in DNS where  $q$  is correlated to  $Q_p$  but in channel flows and Vflame (Gruber et al. 2010; Bruneaux et al. 1996). It is widely accepted that the 'flame' tends to slow down and become laminar near the wall during FWI leading to question the role the turbulence intensity plays on the transport of heat flux during FWI especially in closed chamber combustion. The results show that despite slowing down of flame, turbulence intensity plays a role to enhance  $Q_p$ . Furthermore, we observe that the difference between  $Q_p$  vs  $P_{int}$  curves of the turbulent and laminar case increases with an increase in  $P_{int}$ . We hypothesize that with the increase in  $P_{int}$ , the turbulence eddies near the wall may get compressed leading to a decrease in their characteristic length, increasing the possibility of turbulence eddies to participate in FWI, hence the increased effect of  $q$  on  $Q_p$ .

## 4 Conclusion

In this paper, we have presented the study of FWI of CH<sub>4</sub>-air mixtures ( $\Phi=0.8$ ) in HOQ configuration in a CVC. High-speed surface temperature measurements are employed to compute the heat flux during FWI.  $Q_p$  is the first peak of heat flux during FWI and quenching events. High-speed PIV is carried out to compute the flow field during FWI. With the variation of fan operation in the CVC different turbulent flowfield was obtained leading to both laminar and turbulent combustion regimes in the CVC. The velocity flowfield analysis indicates that in this setup, the FWI occurs in a region of confinement where the mean velocity prior to FWI is near zero. This implies that the different flow field affects the  $Q_p$  during FWI through the variation in  $q$  (not mean velocity). The variation in  $X_D$  led to different  $P_{int}$  in each flow condition.

Analyzing the laminar FWI at different  $P_{int}$ , it is found that  $Q_p$  is proportional to  $P_{int}^b$  where  $b=0.35$ .  $b$  is close to what has been found in the literature. Not only variation in  $X_D$  but also variation in fan operation led to different  $P_{int}$ . Since the experiment conditions (experiment configuration, fuel–air mixture composition, and wall temperatures) remained the same, the power-law dependency obtained in laminar conditions is utilized to separate the effect of  $q$  from  $P_{int}$  in turbulent conditions. Turbulent conditions lead to increase in scatter of  $Q_p$  leading to lack of shot-to-shot correlation between  $q$  and  $Q_p$ . However the mean tendencies show an increase in  $q$  is found to increase  $Q_p$  with a higher value of  $b=0.76$  using power law dependency. These results show that despite flame laminarization,  $q$  plays a role in heat transfer during FWI. The results also indicate the necessity to

explore the mechanism of how does turbulence involve in the transport of heat to the wall during FWI, possibly exploring the turbulent length scales during FWI. Further, the range of  $P_{int}$  and  $q$  could be varied to obtain highly accurate correlations which would be beneficial for the design of new combustion systems.

**Acknowledgements** The authors gratefully acknowledge financial support and access to experiment facilities provided by IFP Energies Nouvelles and ISAE-ENSMA. The authors also acknowledge Clement Bramouille and Jerome ChereI for their help to conduct the experiments.

**Author Contributions** AP conducted the experiments. All the authors were involved in conceptualization and analysis of the experiment data. AP wrote the first draft. All authors contributed to the manuscript reading, revisions, improvements and approved the submitted version.

**Funding** Institut PPRIME, CNRS/ ISAE-ENSMA, Université de Poitiers, France and IFP Énergies nouvelles, Institut Carnot IFPEN Transports Energie, France.

## Declarations

**Conflict of interest** The authors have no relevant financial or non-financial interests to disclose.

**Open Access** This article is licensed under a Creative Commons Attribution 4.0 International License, which permits use, sharing, adaptation, distribution and reproduction in any medium or format, as long as you give appropriate credit to the original author(s) and the source, provide a link to the Creative Commons licence, and indicate if changes were made. The images or other third party material in this article are included in the article's Creative Commons licence, unless indicated otherwise in a credit line to the material. If material is not included in the article's Creative Commons licence and your intended use is not permitted by statutory regulation or exceeds the permitted use, you will need to obtain permission directly from the copyright holder. To view a copy of this licence, visit <http://creativecommons.org/licenses/by/4.0/>.

## References

- Aleiferis, P.G., Behringer, M.K., Malcolm, J.S.: Integral length scales and time scales of turbulence in an optical spark-ignition engine. *Flow Turbul. Combust.* **98**(2), 523–577 (2017). <https://doi.org/10.1007/s10494-016-9775-9>
- Baglione, M.L.: Development of System Analysis Methodologies and Tools for Modeling and Optimizing Vehicle System Efficiency. University of Michigan, Michigan (2007)
- Berlad, A.L., Potter Jr, A.E. Prediction of the quenching effect of various surface geometries. In: Symposium (International) on Combustion, Vol. 5, No. 1, pp. 728–735. Elsevier (1955). [https://doi.org/10.1016/S0082-0784\(55\)80100-2](https://doi.org/10.1016/S0082-0784(55)80100-2)
- Boust, B., Sotton, J., Labuda, S.A., Bellenoue, M.: A thermal formulation for single-wall quenching of transient laminar flames. *Combust. Flame* **149**(3), 286–294 (2007a). <https://doi.org/10.1016/j.combustflame.2006.12.019>
- Boust, B., Sotton, J., Bellenoue, M.: Unsteady heat transfer during the turbulent combustion of a lean premixed methane–air flame. Effect of pressure and gas dynamics. *Proc. Combust. Inst.* **31**(1), 1411–1418 (2007b). <https://doi.org/10.1016/j.proci.2006.07.176>
- Boust, B., Sotton, J., Bellenoue, M.: Unsteady contribution of water vapor condensation to heat losses at flame-wall interaction. In: Journal of Physics: Conference Series, Volume 395, 6th European Thermal Sciences Conference (Eurotherm 2012) 4–7 September 2012, Poitiers, France (2012). <https://doi.org/10.1088/1742-6596/395/1/012006>
- Boust, B.: Etude expérimentale et modélisation des pertes thermiques pariétales lors de l'interaction flamme-paroi instantannaire (2006). <http://www.theses.fr/2006POIT2308>.
- Bradley, D., Lawes, M., Morsy, M.: Measurement of turbulence characteristics in a large scale fan-stirred spherical vessel. *J. Turb.* **20**, 1 (2019)
- Bruneaux, G., Akselvoll, K., Poinsot, T., Ferziger, J.H.: Flame-wall interaction simulation in a turbulent channel flow. *Combust. Flame* **107**(1), 27–44 (1996). [https://doi.org/10.1016/0010-2180\(95\)00263-4](https://doi.org/10.1016/0010-2180(95)00263-4)

- Chang, J., Güralp, O., Filipi, Z., Assanis, D.N., Kuo, T.-W., Najt, P., Rask, R. New Heat Transfer Correlation for an HCCI Engine Derived from Measurements of Instantaneous Surface Heat Flux. In: SAE Technical Paper Series (2004).
- Daniel, W.A.: Flame quenching at the walls of an internal combustion engine. In: Symposium (International) on Combustion, Vol. 6, No. 1, pp. 886–894. Elsevier (1957). [https://doi.org/10.1016/S0082-0784\(57\)80125-8](https://doi.org/10.1016/S0082-0784(57)80125-8)
- Dreizler, A., Böhm, B.: Advanced laser diagnostics for an improved understanding of premixed flame-wall interactions. *Proc. Combust. Inst.* **35**(1), 37–64 (2015). <https://doi.org/10.1016/j.proci.2014.08.014>
- Foucher, F., Burnel, S., Mounaim-Rousselle, C., Boukhalfa, M., Renou, B., Trinité, M.: Flame wall interaction. Effect of stretch. *Experim. Therm. Fluid Sci.* **27**(4), 431–437 (2003). [https://doi.org/10.1016/S0894-1777\(02\)00255-8](https://doi.org/10.1016/S0894-1777(02)00255-8)
- Foucher, F. Etude expérimentale de l'interaction flamme-paroi. Application au moteur à allumage commandé (2002). <http://www.theses.fr/2002ORLE2057>.
- Galmiche, B., Mazellier, N., Halter, F., Foucher, F.: Turbulence characterization of a high-pressure high-temperature fan-stirred combustion vessel using LDV, PIV and TR-PIV measurements. *Exp. Fluids* **55**(1), 1636 (2013). <https://doi.org/10.1007/s00348-013-1636-x>
- García-Oliver, J.M., Malbec, L.-M., Toda, H., Baya, Bruneaux, Gilles.: A study on the interaction between local flow and flame structure for mixing-controlled Diesel sprays. *Combust. Flame* **179**, 157–171 (2017). <https://doi.org/10.1016/j.combustflame.2017.01.023>
- Gatowski, J.A., Smith, M.K., Alkidas, A.C.: An experimental investigation of surface thermometry and heat flux. *Exp. Therm. Fluid Sci.* **2**(3), 280–292 (1989). [https://doi.org/10.1016/0894-1777\(89\)90017-4](https://doi.org/10.1016/0894-1777(89)90017-4)
- Gianfilippo, C., Bruno, C., Alessandro, G.: Highly turbulent counterflow flames: a laboratory scale benchmark for practical systems. *Combust Flame* **156**(9), 1834–1843 (2009). <https://doi.org/10.1016/j.combustflame.2009.03.017>
- Gingrich, E., Ghandhi, J., Reitz, R.D.: Experimental investigation of piston heat transfer in a light duty engine under conventional diesel, homogeneous charge compression ignition, and reactivity controlled compression ignition combustion regimes. *SAE Int. J. Engines* **7**(1), 375–386 (2014). <https://doi.org/10.4271/2014-01-1182>
- Gingrich, E., Janeczek, D., Ghandhi, J.: Experimental investigation of the impact of in-cylinder pressure oscillations on piston heat transfer. *SAE Int. J. Engines* **9**(3), 1958–1969 (2016). <https://doi.org/10.4271/2016-01-9044>
- Goodwin, D.G., Moffat, H.K., Speth, R.L.: Cantera (2017).
- Goolsby, A.D., Haskell, W.W.: Flame-quench distance measurements in a CFR engine. *Combust Flame* **26**, 105–114 (1976). [https://doi.org/10.1016/0010-2180\(76\)90060-2](https://doi.org/10.1016/0010-2180(76)90060-2)
- Greene, M.: Momentum near-wall region characterization in a reciprocating internal-combustion engine. Ph.D.Thesis. University of Michigan. Rackcham School of Graduate Studies, checked on 9/1/2021 (2017).
- Gruber, A., Sankaran, R., Hawkes, E.R., Chen, J.H.: Turbulent flame–wall interaction. A direct numerical simulation study. In *J. Fluid Mech.* **658**, 5–32 (2010). <https://doi.org/10.1017/S0022112010001278>
- Hendricks, T., Ghandhi, J.: Estimation of surface heat flux in IC engines using temperature measurements. Processing code effects. *SAE Int. J. Engines* **5**(3), 1268–1285 (2012). <https://doi.org/10.4271/2012-01-1208>
- IEA: Key World Energy Statistics 2021. IEA, Paris (2021)
- Johnson, B., Edwards, C.: Exploring the pathway to high efficiency IC engines through exergy analysis of heat transfer reduction. *SAE Int. J. Engines* **6**(1), 150–166 (2013). <https://doi.org/10.4271/2013-01-0278>
- Julien, M., Guillaume, P., Julien, S., Marc, B., Fabien, R.: High-frequency wall heat flux measurement during wall impingement of a diffusion flame. *Int. J. Eng. Res.* **22**(3), 847–855 (2021). <https://doi.org/10.1177/1468087419878040>
- Kawaguchi, A., Iguma, H., Yamashita, H.; Nishikawa, N.; Yamashita, C.; Takada, N. et al.: Engine heat loss reduction by thermo-swing wall insulation technology. In : COMODIA (The Proceedings of the International symposium on diagnostics and modeling of combustion in internal combustion engines), vol. 2017.9, A207 (2017).
- Kundu, P.K., Cohen, I.M., Dowling, D.R. (Eds.): *Fluid Mechanics* (Sixth Edition). Academic Press, Boston (2016)

- Labuda, S., Karrer, M., Sotton, J., Bellenoue, M.: Experimental study of single-wall flame quenching at high pressures. *Combust. Sci. Technol.* **183**(5), 409–426 (2011). <https://doi.org/10.1080/00102202.2010.528815>
- Mannaa, O.A., Mansour, M.S., Chung, S.H., Roberts, W.L.: Characterization of turbulence in an optically accessible fan-stirred spherical combustion chamber. *Combust. Sci. Technol.* **193**(7), 1231–1257 (2021). <https://doi.org/10.1080/00102202.2019.1686629>
- Metghalchi, M., Keck, J.C.: Laminar burning velocity of propane-air mixtures at high temperature and pressure. *Combust. Flame* **38**, 143–154 (1980). [https://doi.org/10.1016/0010-2180\(80\)90046-2](https://doi.org/10.1016/0010-2180(80)90046-2)
- Metghalchi, M., Keck, J.C.: Burning velocities of mixtures of air with methanol, isooctane, and indolene at high pressure and temperature. *Combust. Flame* **48**, 191–210 (1982). [https://doi.org/10.1016/0010-2180\(82\)90127-4](https://doi.org/10.1016/0010-2180(82)90127-4)
- Moisy, F.: PIVMat. Version 4.20: MATLAB Central File Exchange (2021). <https://www.mathworks.com/matlabcentral/fileexchange/10902-pivmat-4-20>, checked on 8/6/2021.
- Moussou, J.: Caractérisation expérimentale du flux thermique transitoire pariétal pour différents modes de combustion (2019). <http://www.theses.fr/2019ESMA0010>.
- Padhiary, A.: Analysis of Heat Loss during Flame Wall Interaction of Premixed Propagative Flames and Diffusive Spray Flames (2022). <http://www.theses.fr/2022ESMA0007>.
- Payri, R., Viera, J.P., Wang, H., Malbec, L.-M.: Velocity field analysis of the high density, high pressure diesel spray. *Int. J. Multiphase Flow* **80**, 69–78 (2016). <https://doi.org/10.1016/j.ijmultiphaseflow.2015.10.012>
- Pickett, L.M., Genzale, C.L., Bruneaux, G., Malbec, L.-M., Hermant, L., Christiansen, C., Schramm, J. (2010) Comparison of diesel spray combustion in different high-temperature, high-pressure facilities. <https://doi.org/10.4271/2010-01-2106>
- Poinsot, T., Haworth, D.C., Bruneaux, G.: Direct simulation and modeling of flame-wall interaction for premixed turbulent combustion☆. *Combust. Flame* **95**(1–2), 118–132 (1993). [https://doi.org/10.1016/0010-2180\(93\)90056-9](https://doi.org/10.1016/0010-2180(93)90056-9)
- Poinsot, T., Veynante, D.: *Theoretical and Numerical Combustion*. Edwards (2005). <https://books.google.fr/books?id=cqFDkeVABY0C>
- Senecal, K., Leach, F.: *Racing Toward Zero: The Untold Story of Driving Green* (2021).
- Sotton, J., Boust, B., Labuda, S.A., Bellenoue, M.: Head-on quenching of transient laminar flame: heat flux and quenching distance measurements. *Combust. Sci. Technol.* **177**(7), 1305–1322 (2005). <https://doi.org/10.1080/00102200590950485>
- Sotton, J.: *Interactions entre une combustion turbulente et la paroi dans une enceinte fermée*. Université de Poitiers (2003)
- Wakisaka, Y., Fukui, K., Kawaguchi, A., Iguma, H., Yamashita, H., Takada, N., et al.: Thermo-Swing Wall Insulation Technology;—A Novel Heat Loss Reduction Approach on Engine Combustion Chamber. In: *SAE 2016 International Powertrains, Fuels & Lubricants Meeting*: SAE International (2016).